



Circuit Model for Microstrip Array Antenna with Defected Ground Structures for Mutual Coupling Reduction and Beamforming Applications

Khalid Subhi Ahmad^{1,2}, Fauziahanim Che Seman^{3*}, Shipun Anuar Hamzah³, Goh Chin Hock⁴, Shaharil Mohd Shah¹

¹Communication Engineering Department, Faculty of Electrical and Electronic Engineering, Universiti Tun Hussein Onn Malaysia, Parit Raja 86400, Johor, MALAYSIA

²Department of Electronic Engineering, Northern Technical University, (NTU), 41002 Mosul, IRAQ

³Research Centre in Applied Electromagnetics (EMCentre), Universiti Tun Hussein Onn Malaysia, Parit Raja 86400, Johor, MALAYSIA

⁴Electronics and Communication Engineering Department, Universiti Tenaga Nasional, Kajang 43000, Selangor, MALAYSIA

*Corresponding Author

DOI: <https://doi.org/10.30880/ijie.2021.13.01.010>

Received 23 February 2020; Accepted 29 November 2020; Available online 30 January 2021

Abstract: A microstrip array antenna (MAA) structure incorporated with an orthogonal I-shaped defected ground structure (OI-DGS) was proposed and investigated and its equivalent circuit was created. Reflection losses were simulated and verified with the proposed circuit model using CST Commercial and AWR Microwave Office software. The optimized S_{11} parameter of the model was obtained by tuning the dimensions of the microstrip patch elements in the MAA and the lengths and widths of the slots of defected ground structure (DGS). The proposed equivalent circuit is expected to be useful as a model for the DGS design and to study its behavior. Finally, two prototypes of MAA, without and with OI-DGS, were fabricated by the milling technology and tested. The simulated results showed that -5.53 dB mutual coupling reduction and the measured around -3 dB. The simulated results demonstrate that main beam shifted 43° while the measured main beam shifted 36° .

Keywords: Array antenna, antenna radiation patterns, beamforming, defected ground structure, equivalent circuits, mutual coupling

1. Introduction

Recently, one of the most significant design considerations is to design a microstrip array antenna (MAA) with a defected ground structure (DGS) for beamforming technology rather than employing additional phase shifters, which are massive and complicated. The DGS is a technique incorporated between two radiated elements to shift the main beam by controlling the phase angle of the surface current on the radiator [1]. This work investigates the capability of DGS in mutual coupling reduction and for shifting the main lobe, as an alternative approach to the common method based on phase shifters.

The insertion of DGS in MAA was formerly demonstrated to be capable of reducing the mutual coupling [2],[3], improving antenna cross polarization [4],[5], antenna harmonics reduction [6], designing antenna for multiband operation [7], antenna size reduction[8], designing antenna for wideband applications [9], design circularly polarized microstrip antenna [10], designing bandpass, bandstop filter [11], [12], designing reconfigurable filter for wideband applications [13], designing phase shifter [14], compact couplers [15]. DGS disturbs the current distribution in ground planes, and it modifies the features of a transmission line, like the equivalent inductance and capacitance, to achieve the slow-wave effect, band-stop properties [16], and in [17], DGS used for realizing the high Q-factor. Transmission line like coplanar waveguide and microstrip integrated with DGS produces a slow-wave characteristics reasoned by DGS equivalent capacitive and inductive components. As a cause of this slow-wave effect, the electrical lengths of the microstrip transmission line integrated with DGS are taller than the transmission line without DGS [18]. Furthermore, the phase speed of the wave is decreased and reduces its resonance frequency producing to decrease in element dimension for the frequency of operation [19]. The slow-wave spread in the passband is employed for compressing microwave structures, while the stopband is good to cut off undesirable surface waves [20].

There are many methods to analyse the microstrip patch antennas. The three most popular models are the transmission line model, cavity model, and full-wave model. The first model is the easiest, and it provides good physical vision, but it is less precise and more complicated to use it to model coupling. The cavity model is more precise as compared to the transmission line model, but requires more complex implementation. It also provides good physical vision and is rather difficult to model coupling with it, but it has been used successfully. Full-wave modelling is very precise, very versatile, and can treat single element, finite and infinite arrays, stacked elements, arbitrary-shaped elements, and coupling. However, it is the most complex model and usually provides less physical vision [21]. In this paper, the cavity model is utilized for studying a rectangular patch element and an orthogonal I-shaped DGS (OI-DGS). Furthermore, for discontinuity (steps in width) or (change the width of the transmission line), some of these expressions are based on the full-wave model.

An equivalent circuit model gives further physical insight into the performance of that structure and the way this performance is related to its design parameters. If precise enough, it can be utilized in the design procedure as a quick surrogate for the costly electromagnetic simulations [22]. The development of the equivalent circuit model for this array antenna includes extracting the equivalent circuit model for the array without DGS, only DGS, and for the entire array with DGS. Such models help in the initial design of array antenna incorporated with DGS. Lumped circuit model is derived by separating array antenna with a DGS into different stages that contain a patch without feeding line, feeding transmission line with discontinuity, coupling circuit with ground plane, DGS equivalent circuit, and array antenna with DGS. The circuit model has been simulated and reflection losses are compared with the acquired scattering parameters. An equivalent circuit model enables the study and analysis of the MAA performance with OI-DGS insertion in order to explain the electrical and magnetic coupling between MAA and proposed DGS.

This paper is organized as follows. The geometry and characteristics of the proposed MAA with an OI-DGS are presented in Sections 2, 3, and 4, along with the parametric analysis of OI-DGS. Section 5 presents the AWR Microwave Office simulations to develop a new equivalent circuit model for MAA without OI-DGS, only OI-DGS, and MAA with OI-DGS. The proposed equivalent circuit is used to explain the electrical and magnetic coupling between the MAA and proposed DGS. Section 6 presents the measured results. Finally, conclusions have been presented in Section 7. The equivalent model circuit for MAA with an OI-DGS for mutual coupling reduction and beamforming applications has been proposed and designed. The array exhibits mutual coupling reduction around -5.53 dB and beamforming 43° in the range of 29° without DGS to 346° with DGS.

2. Array Antenna Design

Fig. 1(a) depicts a MAA without DGS. The structure includes a 2×1 rectangular element patch array and a $50\text{-}\Omega$ microstrip feed line on Rogers RT/Duroid 5880 board with ϵ_r of 2.2, loss tangent of 0.009, and substrate thickness of 1.575 mm. The ground plane dimensions are $50\text{ mm} \times 19.55\text{ mm}$. Both elements have equal dimension of width (11.1 mm) and length (10.2 mm) and each is separated by a spacing of 13.9 mm, as illustrated in Table 1. The subminiature A connector (SMA)-port excitation is utilized in simulation. Simulations have been carried out using a frequency domain solver in CST MWS with open (add space) boundary conditions.

Subsequently, an OI-DGS is inserted on the ground plane of the MAA with dimensions of $12.3\text{ mm} \times 7.94\text{ mm}$, as illustrated in Fig. 1(b). The distance between the DGS and the edge of the radiation element is optimized through parametric study to 2.98 mm, as shown in Fig. 1(b). Fig. 1(b) depicts the OI-DGS design. It consists of seven slots, namely a , b , c , and d . There are two slots in each of a , b , and d and only one slot in c , as shown in Fig. 1(c). The lengths of a , b , c , and d are 4.1 mm, 12.3 mm, 5.94 mm, and 3 mm, respectively.

Table 1 - Design specifications of MAA

Parameters	Values	
Substrate type	Roger 5880, loss tangent of 0.0009	
Dielectric constant	2.2	
Centre frequency (GHz)	8.928	
values (mm)	Substrate height (h)	1.575
	Patch thickness	0.035
	W	11.1
	L	10.2
	W _{grd}	50
	L _{grd}	19.55
	R	13.9
	W _g	1.6
L _g	5.1	

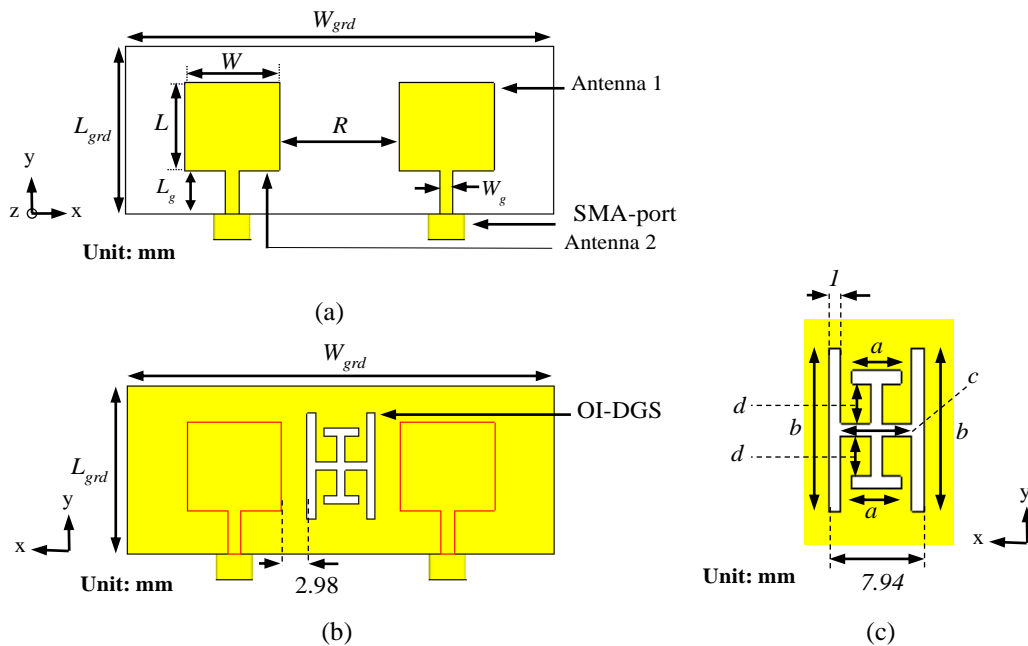


Fig. 1 - Geometry of the (a) MAA without OI-DGS, front view; (b) Proposed MAA with OI-DGS, back view; (c) OI-DGS geometry

3. Simulated Results

The OI-DGS, as illustrated in Fig. 1 (c) with dimensions of 12.3 mm × 7.94 mm, is incorporated on the ground plane between the two radiated elements. The dimension *b* is varied using two different values—8 mm, and 12.3 mm—while maintaining the other values of DGS constant. Fig. 2 illustrates the reflection losses of the planar arrays without DGS, which resonates at 8.928 GHz with a reflection loss of -18.4 dB, whereas the resonant frequency of the antenna arrays shifts from 62 MHz upwards from 8.928 GHz to 8.99 GHz with reflection losses of -15.1 dB after inserting the OI-DGS for *b* = 12.3 mm. The reason beyond frequency shift is due to OI-DGS, which provides a higher Q-factor [17] and slow-wave effect [16]. The detailed changes in the resonant frequency of the rectangular patches are tabulated in Table 2. Subsequent analysis the frequencies 8.93 GHz and 8.99 GHz are considered as resonant frequencies for MAA without and with DGS *b* = 12.3 mm, respectively. The test results of MAA without and with OI-DGS converged after 13 and 15 passes, respectively with a simulation default setting of 2% refinement.

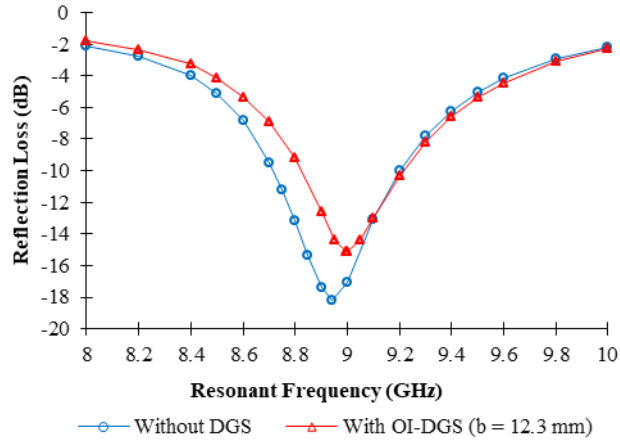


Fig. 2 - Reflection loss of an array antenna with and without the proposed DGS

Table 2 - Change in resonant frequency, f , of the planar arrays for different lengths b

Array type	f for 1 st	f for 2 nd
	Element	Element
MAA without OI-DGS	8.928	8.924
Proposed MAA with OI-DGS, $b=8$ mm	9.01	9.01
Proposed MAA with OI-DGS, $b=12.3$ mm	8.992	8.99

To investigate the effect generated by the OI-DGS and the varying the b dimension, the surface current distribution of the MAA without OI-DGS, MAA with OI-DGS $b=8$ mm, and MAA with OI-DGS $b=12.3$ mm examined, as illustrated in Fig. 3 (a), (b) and (c), respectively. Fig. 3(a) illustrates the simulated surface current distributions for MAA without OI-DGS. At 8.93 GHz, the highest current distribution focuses on the antenna patches and the lower section of the antenna feed line. Fig. 3(b) illustrates the surface current distributions at 9.01 GHz. The highest current focuses on the upper and lower part of OI-DGS slot b and the right and left edge of the antenna patches and antenna feed line. Fig. 3(c) illustrates the surface current distributions at 8.99 GHz. The highest current focuses on the upper and lower part of OI-DGS slot b .

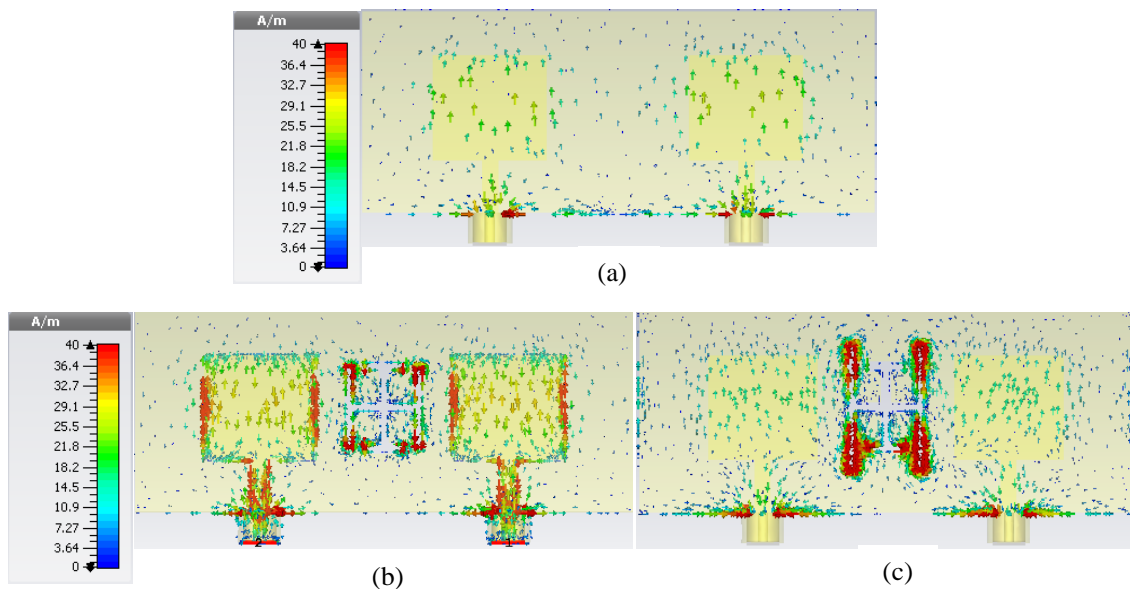


Fig. 3 - Surface current of the MAA (a) without OI-DGS, at 8.93 GHz; (b) with OI-DGS $b=8$ mm, at 9.01 GHz; (c) with OI-DGS $b=12.3$ mm, at 8.99 GHz

4. Beamforming Achievement

The main beam width is comparatively wide owing to the use of only two patches and it is difficult to observe the change in the main beam direction, but this will be more evident by increasing the number of radiated elements. Table 3 reviews the gain of the planar array, angle of main lobe, and gain at the side lobe. Without DGS, the main radiation pattern angle is shifted to 29° at 9.2 dBi with side lobe gain of -6.4 dB. When $b = 8$ mm, the beam direction increases to 25°, as illustrated in Fig. 4(a). The overall gain of the planar array decreases to 8.75 dBi with decrease in the gain at side lobe to -5.6 dB. A significant change in the main beam direction is observed at 346°, when $b = 12.3$ mm, along with an increase in the gain to 9.24 dBi with the side lobe gain of -5.8 dB, as illustrated in Fig. 4(b). The gain increases approximately 0.4 times as compared to the same array antenna without OI-DGS. The influence of the OI-DGS slot is also apparent in reducing the side lobes approximately 9.3 times.

Table 3 - Beam shifting capability for different lengths b

Array type	Gain (dBi)	Main Lobe Direction	Side Lobe (dB)
MAA without OI-DGS	9.2	29°	-6.4
Proposed MAA with OI-DGS, $b=8$ mm	8.75	25°	-5.6
Proposed MAA with OI-DGS, $b=12.3$ mm	9.24	346°	-5.8

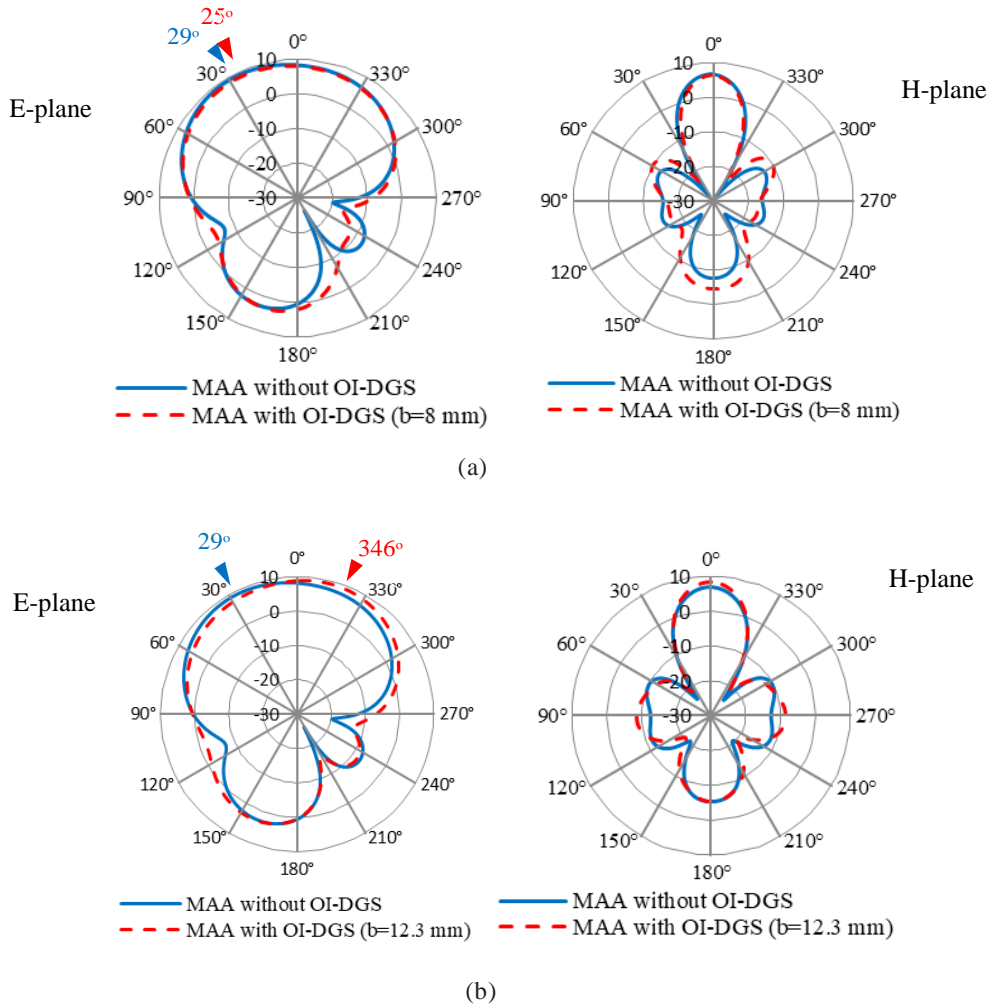


Fig. 4 - Simulated radiation pattern (a) MAA without DGS at 8.93 GHz and with OI-DGS, $b= 8$ mm, at 9.01 GHz, E-plane and H-plane; (b) MAA without DGS at 8.93 GHz and with OI-DGS, $b= 12.3$ mm, at 8.99 GHz, E-plane and H-plane

5. Circuit Model

5.1 Circuit Model for Array Antenna without DGS

The rectangular patches without a feed line are represented by a parallel $R_p L_p C_p$ circuit. Furthermore, this model considers the physical parameters of the structure. An equivalent lumped element of the rectangular patches has been developed using the cavity model. It can be represented as shown in Fig. 5 (a), (b), and (c), where C_p , L_p , and R_p are the equivalent capacitance, inductance, and resistance, respectively, of only the patch without feed line, and their values are determined as follows [23].

$$C_p = \frac{\epsilon_{eff} \epsilon_0 LW}{2h} \cos^{-2} \left(\frac{\pi y_0}{L} \right), \quad (F) \quad (1)$$

$$L_p = \frac{1}{C_p \omega_r^2} \quad (H) \quad (2)$$

$$R_p = \frac{Q_r}{C_p \omega_r} \quad (\Omega) \quad (3)$$

$$Q_r = \frac{v(\epsilon_{eff})^{\frac{1}{2}}}{4f_r h} \quad (4)$$

In these equations, ϵ_{eff} is the effective dielectric constant; ϵ_0 is the permittivity of free-space ($\epsilon_0 = 1/v^2\mu_0$); $\epsilon_0 = 8.85 \times 10^{-12} \text{ F.m}^{-1}$; v is the velocity of electromagnetic waves in free space; L and W represent the length and width of rectangular patch, respectively; y_0 is the inset-fed point position, and in this study, y_0 equals zero; h is the thickness of the substrate; ω_r and Q_r are the angular frequency at resonance [23] and radiation quality factor of the patch, respectively [24]. The resonant frequency is considered to be 8.93 GHz.

Discontinuity indicates a rapid change in the line width at the junction between the patch and feed line. The discontinuity is shown in Fig. 5(a) and it is caused by a sudden change in the geometry of the strip conductor. Further, W represents the width of the wide microstrip section and W_g represents the width of the narrow line section. Notably, the discontinuity causes reflections of the signal with some radiations. The charges increase in the conductor owing to the electric charges that accumulate at the borders of a discontinuity. Consequently, the electric field rises and electric energy is stored. The resulting effect can be represented as a capacitive C_f in the circuit model [25], as shown in Fig. 5(c), where it represents the fringing field capacitance at the junction [25],[26]. Moreover, the discontinuity adjusts the allocation of the current and increases the magnetic field. Magnetic energy is stored in higher-order modes that produce an inductive effect, which can be represented as L_{f1} and L_{f2} in the equivalent circuit model [25], as shown in Fig. 5(c). Therefore, C_f , L_{f1} , and L_{f2} are the equivalent capacitance and inductances of the feed transmission line and discontinuity, respectively. C_f is given as follows [27]:

$$C_f = 0.00137h \frac{(\epsilon_{eff1})^{\frac{1}{2}}}{Z_{c1}} \left(1 - \frac{W_g}{W}\right) \left(\frac{\epsilon_{eff1} + 0.3}{\epsilon_{eff1} - 0.258}\right) \left(\frac{\frac{W_g}{h} + 0.264}{\frac{W_g}{h} + 0.8}\right) \quad (\text{pF}) \quad (5)$$

$$\epsilon_{eff1} = \frac{\epsilon_r + 1}{2} + \frac{\epsilon_r - 1}{2} \frac{1}{\left(1 + 12 \frac{h}{W}\right)^{\frac{1}{2}}} \quad (6)$$

$$Z_{c1} = 120\pi(\epsilon_{eff1})^{-\frac{1}{2}} \frac{1}{\left(\frac{W}{h} + 1.393 + 0.667 \ln\left(\frac{W}{h} + 1.444\right)\right)} \quad (\Omega) \quad (7)$$

where ϵ_{eff1} and Z_{c1} are the effective dielectric constant and characteristic impedance of the rectangular patch, respectively. The factor ϵ_{eff1} depends on the substrate thickness, h , and conductor width, W , L_{f1} and L_{f2} can be calculated from the following equations [25]- [27].

$$L_{f1} = \frac{L_{w1}}{L_{w1} + L_{w2}} L_d \quad (\text{nH}) \quad (8)$$

$$L_{f2} = \frac{L_{w2}}{L_{w1} + L_{w2}} L_d \quad (\text{nH}) \quad (9)$$

where L_{w1} and L_{w2} are the inductance per unit length of the rectangular patch and feed line, with widths of W and W_g , respectively, whereas L_d is the total discontinuity inductance, and is given by [25]- [27].

$$L_{w1} = Z_{c1} \frac{(\epsilon_{eff1})^{\frac{1}{2}}}{v} \quad (\text{H/unit length}) \quad (10)$$

$$L_{w2} = Z_{c2} \frac{(\epsilon_{eff2})^{\frac{1}{2}}}{v} \quad (\text{H/unit length}) \quad (11)$$

where ϵ_{eff2} and Z_{c2} are the effective dielectric constant and characteristic impedance of the feed line, respectively. The units of length used in the equations are metres.

$$\epsilon_{eff2} = \frac{(\epsilon_r + 1)}{2} + \frac{(\epsilon_r - 1)}{2} \frac{1}{\left(1 + 12 \frac{h}{W_g}\right)^2} \quad (12)$$

$$Z_{c2} = 120\pi(\epsilon_{eff2})^{-\frac{1}{2}} \frac{1}{\left(\frac{W_g}{h} + 1.393 + 0.667 \ln\left(\frac{W_g}{h} + 1.444\right)\right)} \quad (\Omega) \quad (13)$$

$$L_d = 0.000987h \left(1 - \frac{Z_{c1}}{Z_{c2}} \left(\frac{\epsilon_{eff1}}{\epsilon_{eff2}}\right)^{\frac{1}{2}}\right)^2 \quad (14)$$

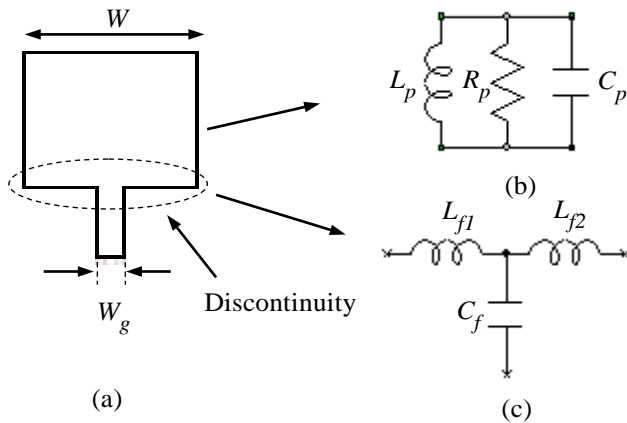


Fig. 5 - Geometry of a single rectangular element and step discontinuity (a) structure; (b) patch circuit model with $L_p = 0.508$ nH, $R_p = 213.139$ Ω , $C_p = 0.625$ pF; (c) feed circuit model with $L_{f1} = 0.00000017549$ nH, $L_{f2} = 0.00000057544$ nH, $C_f = 0.000000088828$ pF

In order to calculate the electromagnetic (EM) coupling and circuit model for DGS, we use a simple idea—(1) and (2) for patches to calculate the EM coupling and (1) to (4) for patches to calculate the DGS circuit model—as will be described in Section 5.2. The two patches are electrically coupled to the ground plane by a coupling circuit (CC), and it can be modelled as a parallel $L_{CC1} C_{CC1}$ resonant circuit. The following parameters are considered for the CC: $L_{CC1} = 0.0547$ nH and $C_{CC1} = 5.7978$ pF at the resonant frequency of 8.93 GHz, as indicated by dotted rectangle in Fig. 6(a). The parameters of the coupling circuit are calculated using (1) and (2), where L and W denote the length and width of the ground plane, respectively.

Fig. 6(a) represents the equivalent circuit for the proposed array antenna without DGS on a Roger board with a substrate thickness of 1.575 mm and permittivity ϵ_r of 2.2. Fig. 6(b) shows the comparison between the reflection loss of the MAA without DGS simulated in CST and the array model circuit simulated by AWR-Microwave Office. The two curves resonate exactly at the same resonance frequency of 8.93 GHz and their -10 dB impedance BW are 476 MHz (8.704–9.18) GHz with BW 5.32% for the CST curve simulation and 280 MHz (8.79–9.07) GHz with BW 3.13% for the circuit model curve extracted by AWR-Microwave Office. The difference between the two curves at 8.93 GHz is approximately 4.677 dB. Generally, it can be observed that the two curves are consistent with each another.

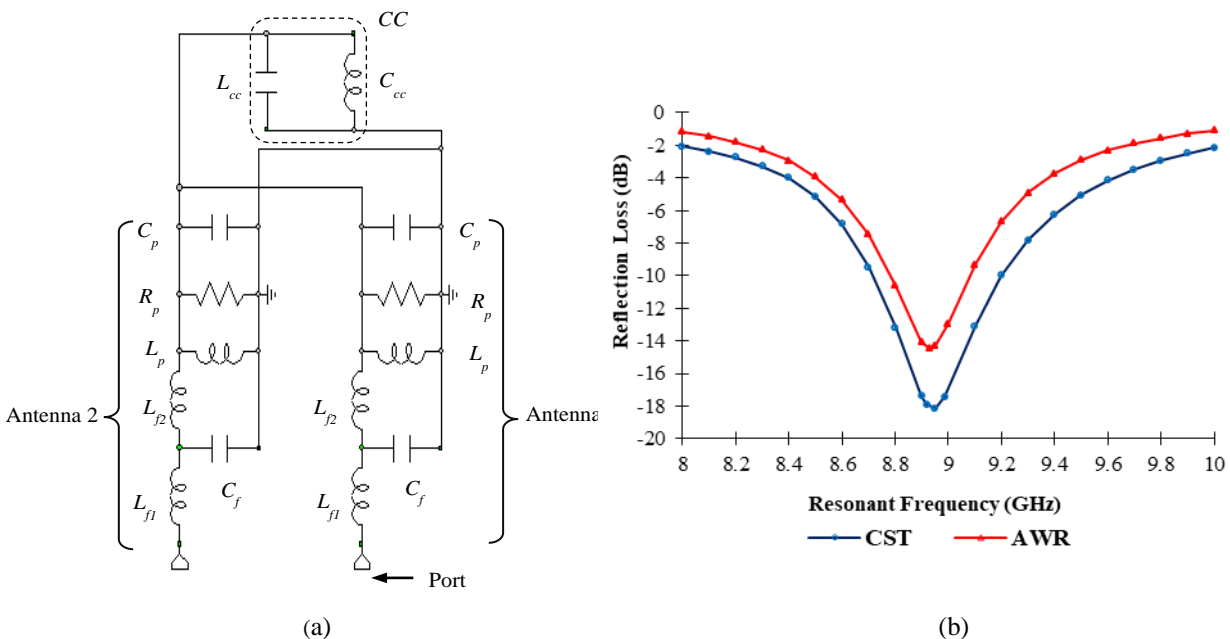


Fig. 6 - (a) equivalent circuit of the array antenna without DGS with $L_{CC1} = 0.0547$ nH, $C_{CC1} = 5.797$ pF, $C_p = 0.625$ pF, $R_p = 213.139$ Ω , $L_p = 0.508$ nH, $L_{f1} = 0.00000017549$ nH, $L_{f2} = 0.00000057544$ nH, $C_f = 0.000000088828$ pF; (b) reflection loss of array antenna without DGS simulated in CST and reflection losses for equivalent circuit simulated in AWR-Microwave Office

5.2 Proposed Orthogonal I-shaped Circuit Model

The proposed DGS model, as illustrated in Fig. 1(c), consist of seven slots, namely a , b , c , and d . There are two slots in each of a , b , and d and only one slot in c . The lengths of a , b , c , and d are 4.1 mm, 12.3 mm, 5.94 mm, and 3 mm, respectively. To study the DGS characteristics, in CST the open (add space) borders are selected at the top and bottom sides in the z -direction. In the x - and y -direction, with the electric boundary condition, $\text{Etan}=0$, and magnetic boundary condition, $\text{Htan}=0$, the waveguide port excitation is used in simulation to obtain the OI-DGS characteristics. Significant beamforming becomes evident when the DGS resonates at the same or approximately same resonant frequency of the array antenna without DGS [28]. The proposed DGS resonates at the frequency of 8.932 GHz, which is close to the resonant frequency of the MAA without DGS.

To benefit from the DGS characteristics, an idea based on integrating DGS into the ground plane between the two patches to shift the resonant frequency of the MAA, thereby shifting the antenna beam angle. To understand the design procedure of the proposed OI-DGS, a parametric study was realized to choose the suitable values of a , b , c , and d .

Fig. 7 (a) and (b) show the identical board size used for MAA, incorporating only a vertical and horizontal slot with a constant width of 1 mm and varying lengths. The location of the slot was in the center of the inter-element spacing between two patches.

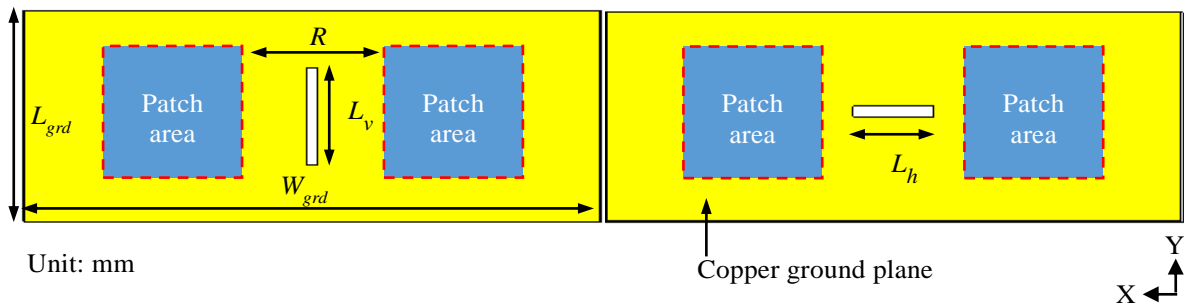


Fig. 7 - The configuration of the DGS (a) vertical slot; (b) horizontal slot

Fig. 8 (a) shows that the reflection losses of the 6 mm, 8 mm and 9 mm vertical slot length (L_v) were higher than the reflection losses of the horizontal slot lengths (L_h) of 3 mm, 5 mm, and 7 mm, as shown in Fig. 8 (b). To decrease DGS resonant frequency, it is observed that combining horizontal and vertical slots reduces DGS resonant frequency and improves reflection loss. A horizontal slot with $L_h = 5.94$ mm was combined with two vertical slots with $L_v = 12.3$ mm, as shown in Fig. 9 (a). The new DGS slot shape, symbolized by (H-DGS). The H-DGS resonant frequency shifted downwards to 9.22 GHz with a reflection loss of -36.17 dB, as shown in Fig. 10(a). Changing DGS dimensions in the x -axis strictly regulated the distance between DGS and the edge of the patch, which has a significant impact on the beam orientation. Thus, this distance was accurately selected after comprehensive simulations. Furthermore, it was observed that it is necessary to leave a separation distance between the edge of the patch and DGS to ensure that the patches operate correctly. Decreasing DGS resonant frequency to be close to or equal to the MAA resonant frequency requires increasing its size either horizontally or vertically. Because there is not enough horizontal space, it is only possible to enlarge its dimension in the vertical direction. Fig. 9 (b) shows that by adding two vertical slots with a length of 3 mm or as symbolized by DGS shape-a, the structure shape-a resonant frequency shifted downward again to 9.18 GHz with reflection loss of -36.80 dB, as shown in Fig. 10(a). It is necessary to add an upper horizontal slot with 4.1 mm length, as shown in Fig. 9 (c), symbolized by DGS shape-b, to increase DGS frequency drop. The DGS resonant frequency shifted downward to 9 GHz with a reflection loss of -36.84 dB, as shown in Fig. 10(a). Finally, Fig. 1(c) shows that by adding the lower horizontal slot, the OI-DGS resonant frequency shifted to 8.932 GHz with a reflection loss of -39 dB, which is close to the resonant frequency of the MAA without DGS, as shown in Fig. 10(a). For investigating the effect of varying the dimension b on the OI-DGS resonant frequency, b changed using four different values, 8 mm, 12.3 mm, 14 mm, and 15 mm, while maintaining the other values in Fig. 1(c) constant. The resonant frequency of the OI-DGS falls between 8.03 GHz and 9.37 GHz when b increases from 8 mm to 15 mm, as illustrated in Fig. 10 (b).

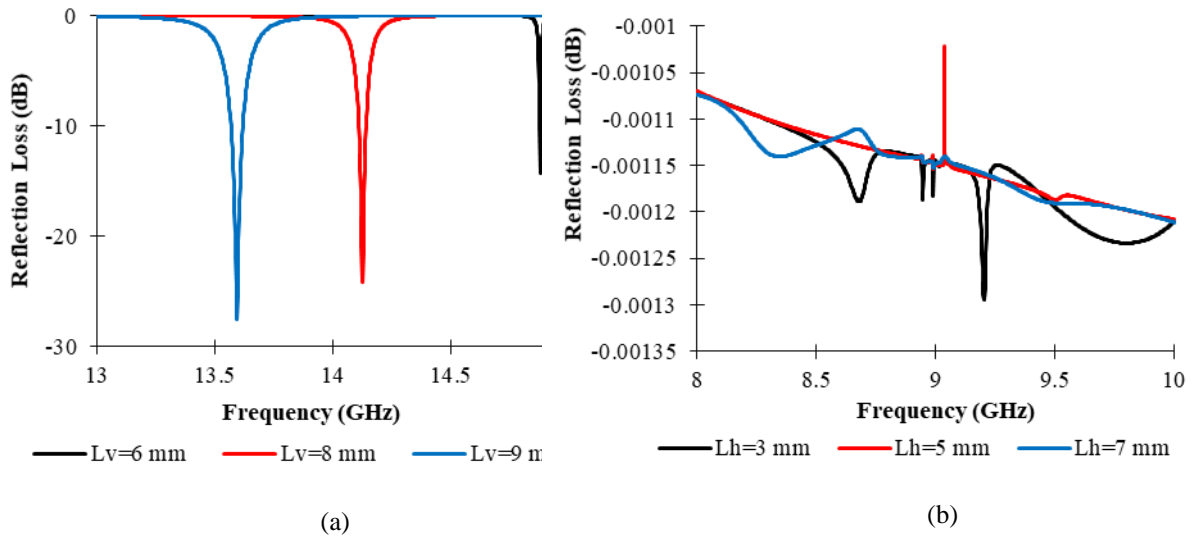


Fig. 8 - Reflection loss of the (a) vertical slot; (b) horizontal slot

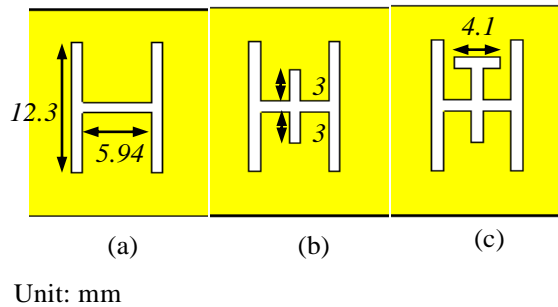


Fig. 9 - The configuration of the (a) H-DGS; (b) DGS shape-a; (c) DGS shape-b

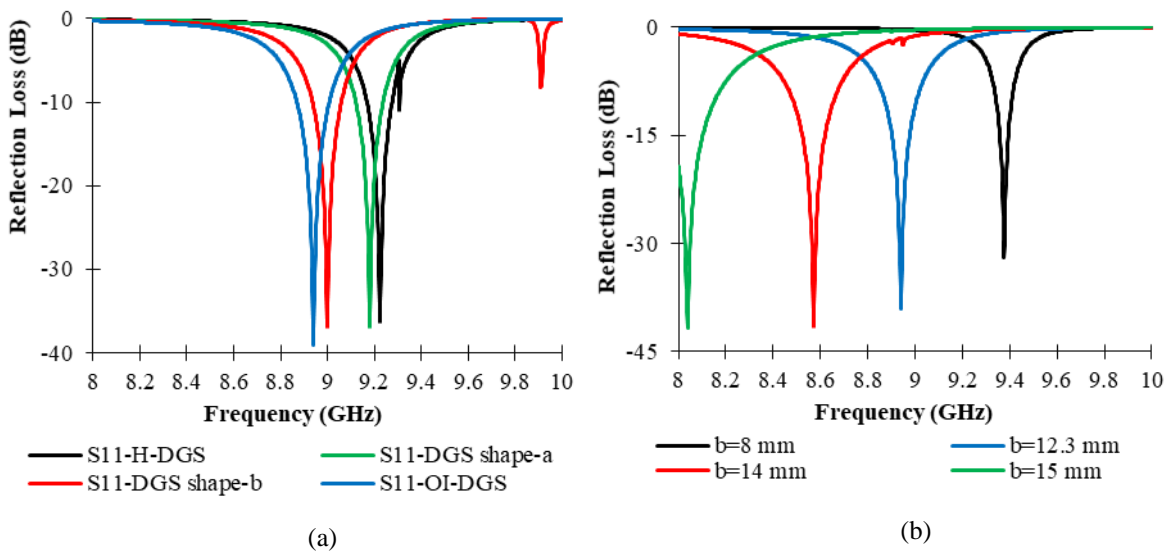
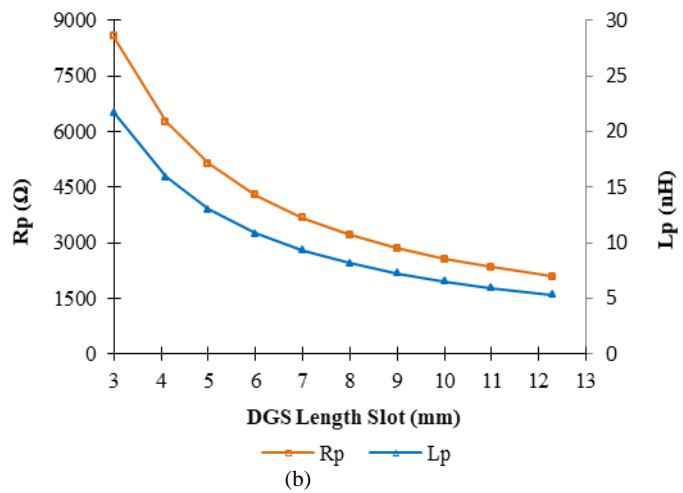
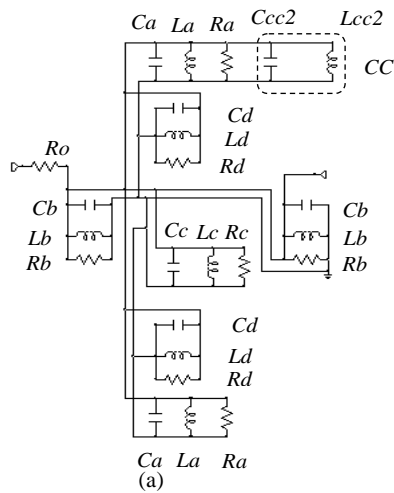


Fig. 10 - (a) the DGS reflection loss for different DGS structures; (b) the OI-DGS reflection loss for different b values

The circuit model of each slot acts as a parallel (R_p, L_p, C_p) circuit connected in parallel. The values of C_p, L_p , and R_p are the same for the same slot length and can be calculated from (1) to (4). Further, L and W represent the length and width of slots, respectively, and the width of slots is 1 mm. Further, considering that the DGS acts as a CC on the ground plane since it is etched in the ground plane, it can be represented as $Lcc2Ccc2$ resonant circuit, which is connected in parallel with the DGS model. The parameters of the CC are given as follows: $Lcc2 = 0.0547$ nH, $Ccc2 = 5.797$ pF at the DGS resonance frequency of 8.932 GHz, and L and W denote the length and width of the ground plane, respectively. Moreover, there are a few losses represented by series $R_o = 5 \Omega$. It represents additional losses in the equivalent circuit model. It has been introduced as parameter to provide a closer agreement between the proposed equivalent circuit model and simulation results.

Fig. 11(a) illustrates the DGS equivalent circuit with extracted (R_p, L_p, C_p) values for each slot. In order to demonstrate the relationship of OI-DGS with (R_p, L_p, C_p), Fig. 11(b) and (c) show the relationships based on changing the physical dimensions of the DGS slot with values of (R_p, L_p, C_p), while maintaining the width of the slot constant at 1 mm. Fig. 11(b) and (c) indicate the variations of (R_p, L_p, C_p) with respect to different the DGS slot lengths from 3 mm to 12.3 mm. It can be observed that both R_p and L_p decrease with the slot dimension. For instance, when the slot length increases from 7 mm to 8 mm, R_p and L_p decline from 3667.63 Ω to 3209.18 Ω and from 9.307 nH to 8.144 nH, respectively, as shown in Fig. 11(b); however, these relationships are not linear. In contrast, and for the same instance, C_p has an opposite behaviour with a linear relationship. Its value increases from 0.0341 pF to 0.0389 pF, as shown in Fig. 11(c).

Fig. 12(a) illustrates the OI-DGS ($b = 12.3$ mm) characteristic comparison between the reflection loss for DGS characteristics extracted from CST and the DGS model circuit simulated by AWR-Microwave Office. The reflection loss curve obtained in the numerical analysis in AWR-Microwave Office trend experiences an upward shift, which is at a maximum near the resonant frequency of 8.932 GHz. The reason for the discrepancy will be illustrated in Section 5.3. Fig. 12(b) shows the comparison between the reflection phase of OI-DGS ($b = 12.3$ mm) simulated in CST and the OI-DGS model circuit simulated in AWR-Microwave Office. It can be observed that both the reflection phase curves are consistent with each other. The slight difference observed in the simulated DGS reflection magnitude and circuit model reflection phases is due to the differences in the degraded performance of simulated DGS reflection magnitude and the equivalent circuit model.



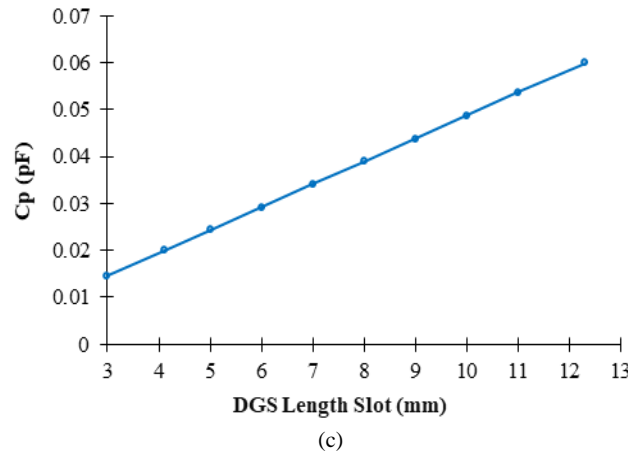


Fig. 11 - (a) DGS equivalent circuit with $L_{cc2} = 0.0547$ nH $C_{cc2} = 5.797$ pF, $C_a = 0.0199$ pF, $L_a = 15.891$ nH, $R_a = 6261.805$ Ω , $C_b = 0.0599$ pF, $L_b = 5.297$ nH, $R_b = 2087.268$ Ω , $C_c = 0.0292$ pF, $L_c = 10.858$ nH, $R_c = 4278.900$ Ω , $C_d = 0.0146$ pF, $L_d = 21.717$ nH, $R_d = 8557.801$ Ω , $R_o = 5$ Ω ; (b) variations of R_p and L_p with different slot lengths; (c) variations of C_p with different slot lengths

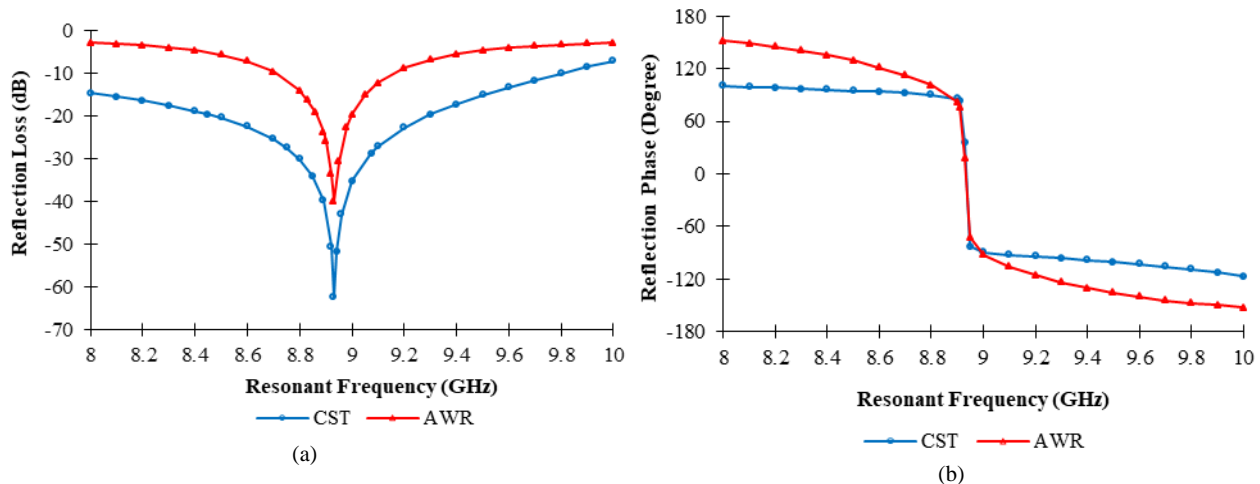


Fig. 12 - Comparison of OI-DGS ($b = 12.3$ mm) characteristics (a) reflection loss using CST MWS and AWR Microwave Office; (b) reflection phase using CST MWS and AWR Microwave Office

5.3 Circuit Model for Array Antenna with DGS

The mutual coupling between the elements in the array antenna causes a small shift of the resonant frequency of the single element. The single element of the antenna resonates at 9.022 GHz, but when two elements are combined together as an array, the resonant frequency is shifted downwards by as much as 92 MHz. This is common when a DGS is embedded in an antenna array as it modifies the resonant frequency [28], owing to the electrical coupling with both the rectangular patches and ground plane. It can be modelled as a parallel $L_{cc3} C_{cc3}$ resonant circuit connected to both the rectangular patches and DGS at its both sides, as indicated by the dotted rectangle in Fig. 13(a). The values of L and W in (1) denote the length and width of ground plane, respectively. The given parameters of the CC are: $L_{cc3} = 0.054$ nH, $C_{cc3} = 5.797$ pF at the resonant frequency of 8.99 GHz. The simulated results showed that varying the ground plane dimensions changes the resonant frequency of DGS and array antenna.

Fig. 13(b) shows the reflection loss of MAA with OI-DGS simulated using CST and those of the equivalent circuit with OI-DGS simulated using AWR-Microwave Office. The two curves resonate exactly at the same resonant frequency of 8.99 GHz and their -10 dB impedance BW are 384 MHz (8.82–9.204) GHz with a BW of 4.26% for the CST curve simulation and 280 MHz (8.84–9.12) GHz with BW of 3.11% for the circuit model curve extracted by AWR-Microwave Office. The difference between the two curves is at approximately 2 dB at 8.99 GHz.

The difference between the results obtained from the CST MWS and AWR-Microwave Office is shown in Fig. 6(b), 12(a) (b), and 13(b) and it is very likely that, during numerical analysis, some of the parameters have not been

catered, such as the distance between the two patches R , the difference between SMA-port used in CST MWS and the port in AWR Microwave Office, and the boundary conditions, which might also have affected the reflection loss. Thus, the reflection loss value at a resonant frequency cannot be accurately represented. Furthermore, another important reason for the inaccuracies in the results of Fig. 6(b) and 13(b) is that, according to (14), there is an error that depends on the values of W , W_g , and h , as was briefly mentioned in [25].

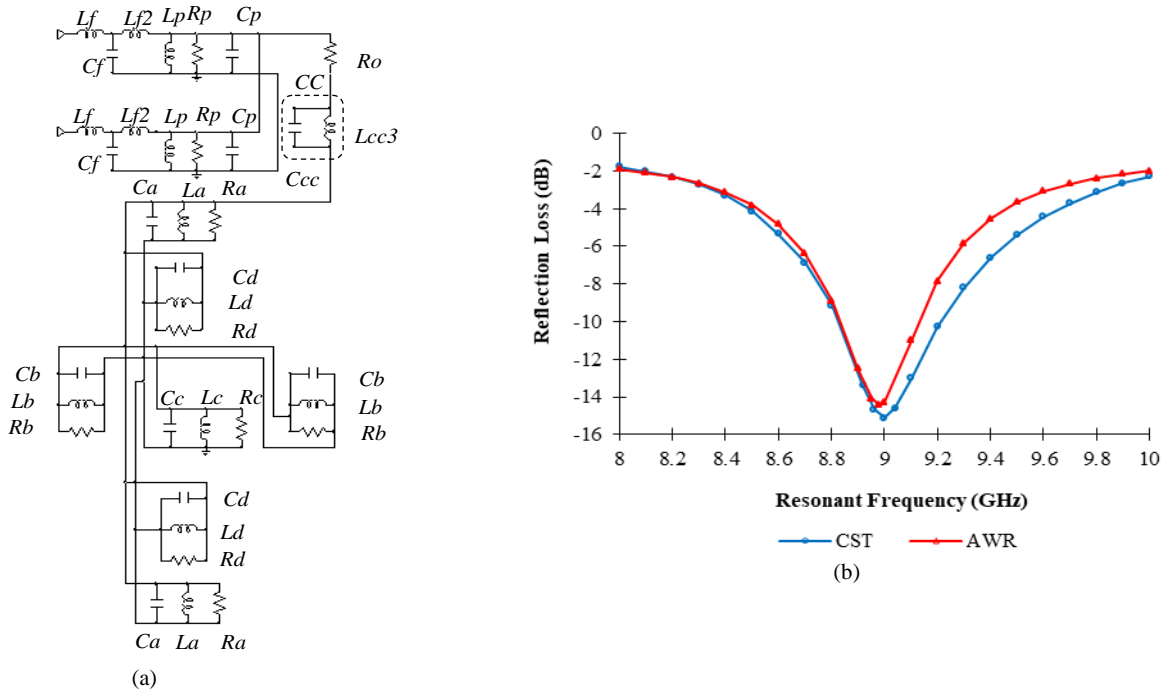


Fig. 13 - (a) equivalent circuit of MAA with OI-DGS with $L_{cc3} = 0.054$ nH, $C_{cc3} = 5.797$ pF, $C_p = 0.625$ pF, $R_p = 213.139$ Ω , $L_p = 0.508$ nH, $L_{f1} = 0.00000017549$ nH, $L_{f2} = 0.00000057544$ nH, $C_f = 0.00000088828$ pF, $C_a = 0.0199$ pF, $L_a = 15.891$ nH, $R_a = 6261.805$ Ω , $C_b = 0.0599$ pF, $L_b = 5.297$ nH, $R_b = 2087.268$ Ω , $C_c = 0.0292$ pF, $L_c = 10.858$ nH, $R_c = 4278.900$ Ω , $C_d = 0.0146$ pF, $L_d = 21.717$ nH, $R_d = 8557.801$ Ω , and $R_o = 5$ Ω ; (b) reflection loss for MAA with the proposed OI-DGS, simulated with both software packages

Table 4 shows the comparison between the four various approaches and the proposed in this paper. In [29] proposed LC and RLC method, which is specific to the dumbbell DGS analysis and for DGS that have an identical shape such dumbbell DGS where they have the same properties as dumbbell DGS and so can analyze. The π shaped proposed by [30] has more accurate results in comparison with LC and RLC circuits. The common disadvantages in LC and RLC, π , and in the Quasi-static method is that they cannot determine the location of DGS on the ground plane. Furthermore, an advantage observed with the ideal transformer method is that it can determine the location of DGS.

Table 4 - Comparison of parameter derivation methods from literature vs. proposed method

Method	Advantage	Disadvantage
LC and RLC [29]	DGS, which have an identical shape such as dumbbell DGS have nearly the same characteristics such as dumbbell DGS and could be analyzed.	Difficult, Cannot decide the location of DGS.
π shaped [30]	More precisely, results compared with LC and RLC.	Difficult, Cannot decide the location of DGS.
Quasi-static [31]	This method directly derived the equivalent circuit model from the physical dimensions of the DGS.	Difficult, Cannot decide the location of DGS.
Ideal transformer [32]	Able to decide the location of DGS.	-----
This work	Easy method with high accuracy.	Cannot decide the location of DGS.

6. Measured Results

For validation purposes, two MAA prototypes have been fabricated by milling, based on the geometrical dimensions described in Table 1. One is without DGS, and one is with DGS for ($b = 12.3$ mm), based on the DGS geometrical dimensions described in Section 5.2. The substrate used is Rogers RT/Duroid 5880, with ϵ_r of 2.2, loss tangent of 0.009, and a substrate thickness of 1.575 mm.

The prototypes were experimentally tested using a vector network analyser, Agilent N5242A, for measuring reflection losses, and an anechoic chamber employing the Agilent E5071C (300 KHz-14GHz) network analyser for far-field pattern measurements. Photographs of the fabricated prototypes are shown in Fig. 14(a) and (b). The measurements were implemented using a high precision test cable with 3.5 mm precision connectors, as shown in Fig. 14 (c). The analyser was calibrated using the Agilent N4433A calibration kit. Two ports of the network analyser were used for measurements. Fig. 14(d) shows the MAA on the rotating position system in an anechoic chamber. The prototypes were rotated in 1° increments during the pattern measurement.

As mentioned at the end of Section 3, the frequencies 8.93 GHz and 8.99 GHz are considered as resonant frequencies for MAA without and with DGS $b = 12.3$ mm, respectively; However, as illustrated in Table 2, antenna 1 and 2 resonate at 8.928 GHz and 8.924 GHz, respectively, for the array without DGS, and at 8.992 GHz and 8.99 GHz, respectively, for the array with DGS.

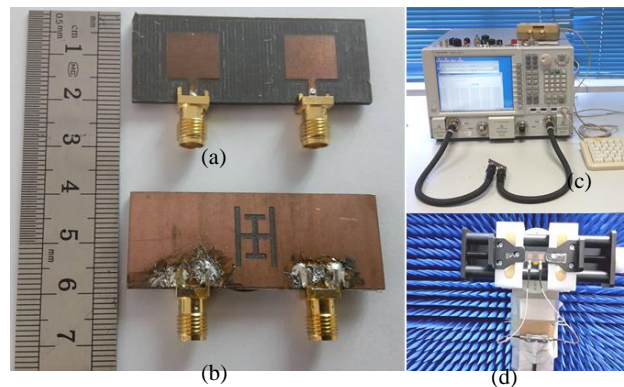


Fig. 14 - The configuration of the two prototypes (a) array without DGS (top view); (b) array with DGS $b = 12.3$ mm (bottom view); (c) photograph of the array under test in the measurement setup; (d) photograph of the array under test in an anechoic chamber

Fig. 15 (a) shows the comparison of reflection loss between the simulated and the measured results for MAA without DGS. The simulated S_{11} (antenna 1) was centred at 8.928 GHz, with a reflection loss of -18.4 dB, and the S_{22} (antenna 2) was centred at 8.924 GHz, with a reflection loss of -18.18 dB. Further, the measured S_{11} was centred at 9.092 GHz with a reflection loss of -15.37 dB and the S_{22} was centred at 9.15 GHz with a reflection loss of -14.7 dB. The percentage error of the resonant frequency shift for S_{11} and S_{22} is 1.83 % and 2.53 %, respectively. The impedance BW of the simulated S_{11} and S_{22} are 476 MHz and 472 MHz, respectively. Further, for the measured results, S_{11} and S_{22} are 358 MHz and 342 MHz, respectively.

Fig. 15(b) shows the comparison of reflection loss between the simulated and the measured results for the array with DGS ($b = 12.3$ mm). The simulated S_{11} was centred at 8.992 GHz, with a reflection loss of -14.96 dB, and the S_{22} was centred at 8.99 GHz, with a reflection loss of -14.84 dB. Further, the measured S_{11} was centred at 9.08 GHz, with a reflection loss of -14.23 dB, and the S_{22} was centred at 9.1 GHz, with a reflection loss of -13.67 dB. The percent error of the resonant frequency shift for S_{11} and S_{22} is 0.97 % and 1.22 %, respectively. The impedance BW of the simulated S_{11} and S_{22} are 384 MHz and 386 MHz, respectively. Further for the measured results, S_{11} and S_{22} are 318 MHz and 296 MHz, respectively. The reflection loss results from S_{11} and S_{22} in Fig. 15 (a) and (b) investigated, as listed in Table 5. There are some differences between the results simulated by CST and those measured, but generally, they are in quite good agreement. The differences are mainly due to manufacturing and assembling tolerances.

The proposed DGS dimensions and the distance between the DGS and the edge of the radiation element (2.98 mm) in Fig. 1 (b) are optimised to provide maximum beamforming and mutual coupling reduction. The mutual coupling reduction between the two elements is observed at -5.82 dB at the resonant frequency of 9.01 GHz, and -5.53 dB at the resonant frequency of 8.99 GHz for two different values of b 8 mm and 12.3 mm, respectively, as mentioned previously in Table 2.

It is found that significantly increased isolation can be obtained between a pair of patches with the edge to edge a distance of 0.41λ at frequency 8.9 GHz where λ is the free space wavelength [33]. Then by integrating the OI-DGS for a distance of $\lambda/11.41$ between patch edges to DGS edge for different b dimensions (8 mm and 12.3 mm). Therefore, mutual interaction between the two elements is observed at -5.82 dB, -5.53 dB, for different values of b 8 mm, and 12.3 mm, respectively. Fig. 15(c) shows the comparison between simulated and measured mutual coupling for an array without and with OI-DGS for $b = 12.3$ mm. The simulated results showed that around -5.53 dB mutual coupling reduction for an array with DGS is achieved at the resonant frequency, 8.99 GHz. The measured results showed that around -3 dB mutual coupling reduction within the impedance BW has been achieved by employing OI-DGS.

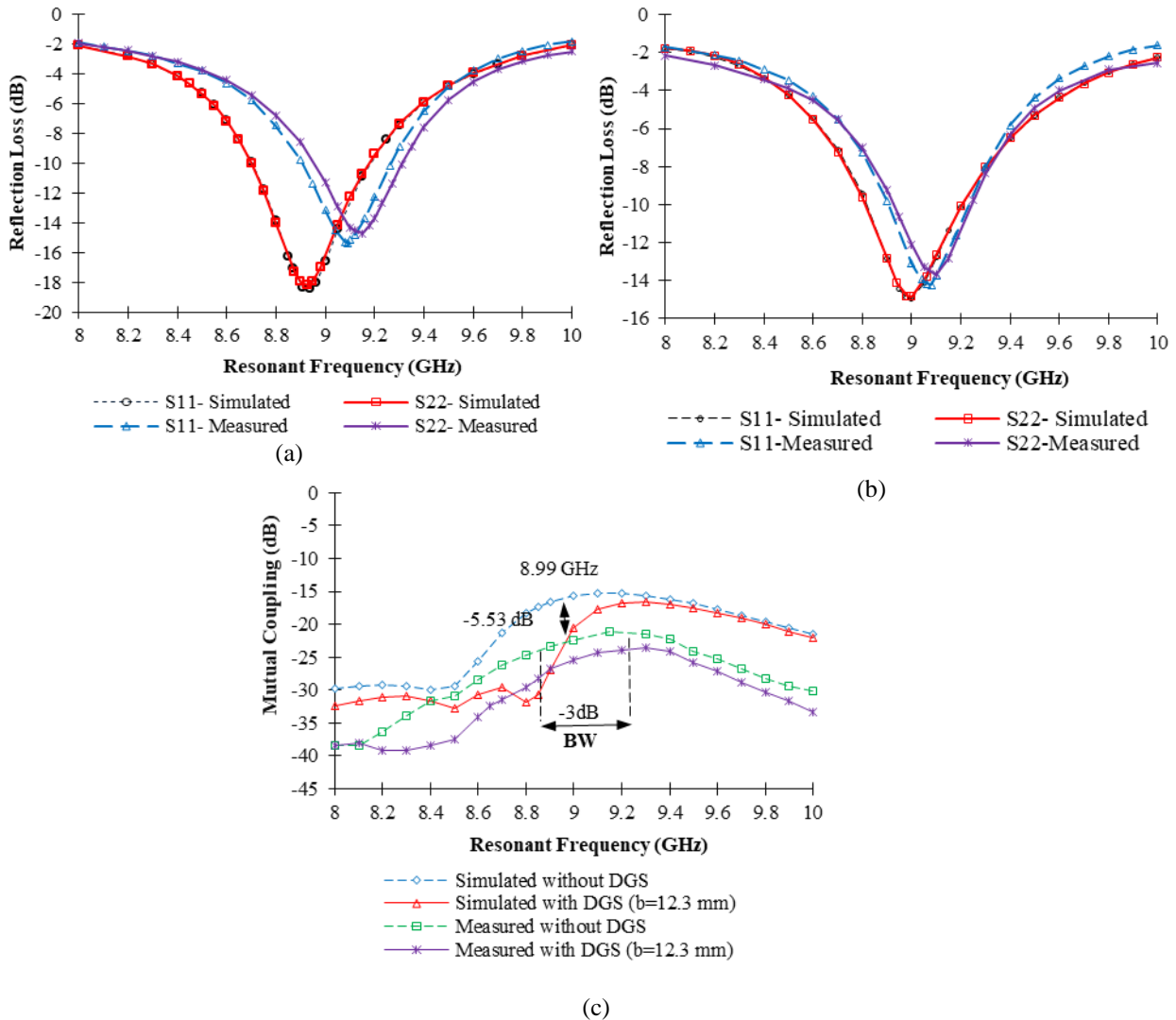


Fig. 15 - comparison CST simulated and measured MAA (a) reflection loss without DGS; (b) reflection loss with DGS $b = 12.3$ mm; (c) Mutual coupling without and with DGS, $b = 12.3$ mm

The simulated and measured radiation patterns in two the standard plane, namely, the E-plane (y-z-plane) and H-plane (x-z-plane) of the proposed MAA at two cases (Case-1 and Case-2), as shown in Table 5, were normalized and plotted in Fig. 16. The simulated main beam shifted 43° from 29° to 346° while the measured main beam shifted 36° from 16° to 340° . The difference between the simulated and measured results is only 7° thus indicates a good agreement in both.

Table 5 - Simulated and measured resonance frequencies, and bandwidth

Case	Antenna	Resonance frequencies (GHz)				Bandwidth (MHz)			
		Simulated		Measured		Simulated		Measured	
		S_{11}	S_{22}	S_{11}	S_{22}	S_{11}	S_{22}	S_{11}	S_{22}
Case-1	MAA without OI-DGS	8.928	8.924	9.092	9.15	476	472	358	342
Case-2	MAA with OI-DGS ($b=12.3$ mm)	8.992	8.99	9.08	9.1	384	386	318	296

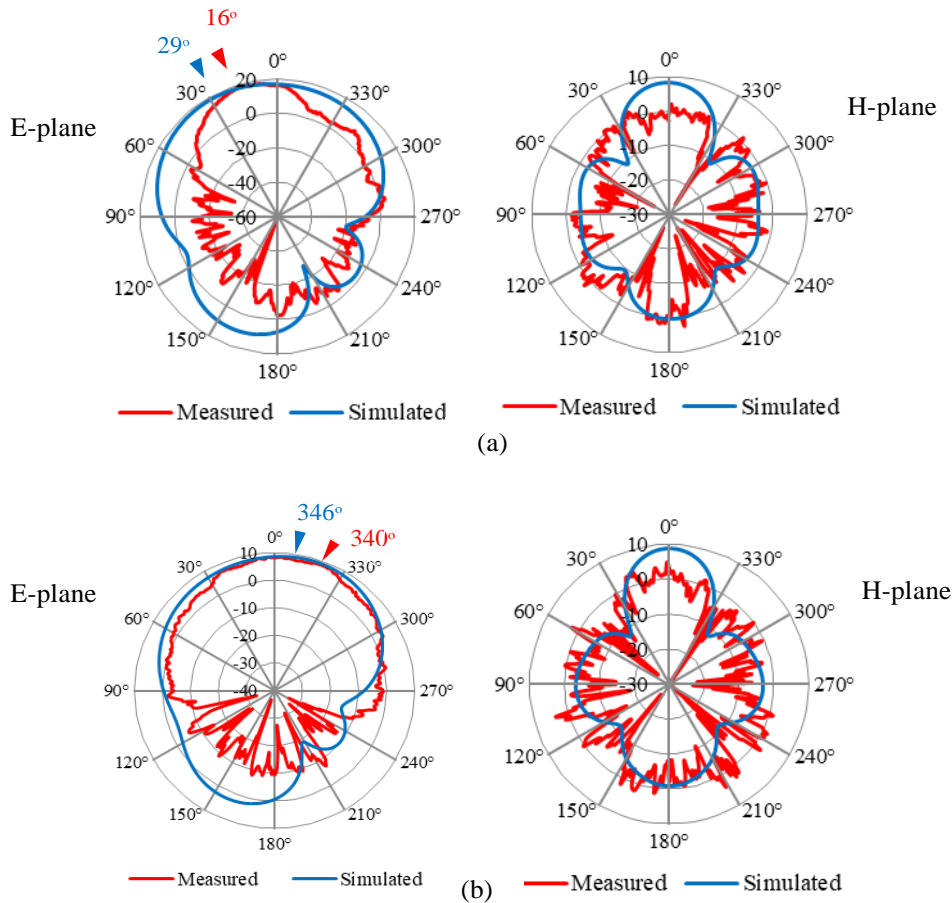


Fig. 16 - Simulated and measured radiation pattern of Case-1 and Case-2 (a) Case-1 simulated at 8.93 GHz and measured at 9.09 GHz, E-plane and H-plane; (b) Case-2 simulated at 8.99 GHz and measured at 9.08 GHz, E-plane and H-plane

Table 6 compares the newly evolved antenna announced in the literature and the proposed MAA in terms of complexity, size, operating frequency, gain, beamforming angle, and substrate material. As illustrated in Table 6, the antenna in [34], [35], [36] has broad-angle scanning ability when antenna construction is more complicated compared with the proposed MAA, which has a simple design and comparatively small size.

Table 6 - Comparison between proposed MAA and literature

Ref. No.	Antenna construction	Complexity	Antenna size (mm ²)	Operating frequency (GHz)	Gain (dBi)	Beamforming (θ°)	Substrate material
[34]	Element is composed of four similar arc dipoles feed by a broadband feeding network.	High	75x75	2.45	4.11	0°, 90°, 180°, 270°	Rogers 4350B
[35]	Dual dipole arms separated by decoupling network feed by phase synthesized transmission lines and Wilkinson power divider.	High	65x65	2.4	4	0°, 30°, 90°, 270°, 330°	Rogers 4003C
[36]	Dual horizontally placed substrates, vertically inserted T-shape feed substrate, and four posts	Medium	55x70	2.45	4.9-6.7	0°, 45°, 90°, 270°, 315°	Rogers Duroid 5880
[37]	Antenna consists of four main parts: the corrugated crossed slot, four parasitic slots, the feed, and the reflective surface	High	235x235	0.7-0.9	7.8-9.3	0°, 30°, 330°	FR4-RO4003
[38]	Slot antenna with an aluminum plate as a reflector	Medium	130x304	1.79, 1.89, 2.07	3.3-6.3	0°, 15°, 345°	Taconic RF35
[39]	Element composed of a loop and a monopole antenna	Medium	50x14	2.4, 3.4	1.26-1.43	30°, 210°, 270°	FR-4
[40]	Patch element as a driven element, surrounded by parasitic elements	Medium	60x42	5.7	9.5	40°, 320°	Rogers R03003C
[41]	1x2 Rectangular patch	Medium	151.5x160.9	2.15, 2.27, 2.38	7.7-8.5	23°, 337°	Rogers Duroid 5880
[42]	Top-loaded monopole antenna fed by a CPW line	Medium	90x85	2.3, 2.7	4.05	30°, 345°	FR-4
This work	1x2 Rectangular patch	Low	50x19.55	8.9, 8.99	9.2-9.24	29°, 346°	Rogers Duroid 5880

7. Conclusion

A design of 2×1 rectangular patches integrated with OI-DGS slot has been presented. The equivalent circuit model of the array antenna with and without DGS is derived. This model is obtained by studying scattering parameters (S_{11}) of the antenna array, antenna array with DGS, and DGS characteristics. Further improvement on the circuit model can be realized by inserting LC coupling circuit between the resonant stage of array antenna and resonant stage of DGS. The LC coupling circuit is the key parameter in determining the resonance frequency; further, any additional DGS can shift the frequency.

This is an improved equivalent circuit parameters extraction method for the proposed DGS and the results indicate fairly good consistency between both simulation software programs.

Two prototype MAA s, without and with DGS ($b = 12.3$ mm), have been fabricated and tested. The simulated and measured results were compared, and the agreement is satisfactory.

Acknowledgement

This work was supported in part by the Office for Research, Innovation, Commercialization, and Consultancy (ORICC), Universiti Tun Hussien Onn Malaysia (UTHM) under Graduate Research Incentive Grant Scheme, GIPS /2015/ U278, Research and Innovation Fund E1550.

The authors would like to thank Universiti Tenaga Nasional (UNiTEN) and especially Dr. Goh for the opportunity to use the powerful design tool AWR Microwave Studio. The authors also thank the Assistant Engineers, Nazri and Sufian, of UTHM and UTeM, for their help with the manufacturing and measurements, respectively.

References

- [1] C. Garg, and M. Kaur. (2014). A review of defected ground structure (DGS) in microwave design, *Int. J. Innov. Res. Electr. Electron. Instrum. Control Eng.*, vol. 2, pp. 1285-1290
- [2] K. Wei, J. Li, L. Wang, Z. Xing, and R. Xu. (2016). S-shaped periodic defected ground structures to reduce microstrip antenna array mutual coupling, *Electron. Lett.*, vol. 52, no. 15, pp. 1288–1290
- [3] E. Fritz-Andrade, A. Perez-Miguel, R. Gomez-Villanueva, and H. Jardon-Aguilar. (2020). Characteristic mode analysis applied to reduce the mutual coupling of a four-element patch MIMO antenna using a defected ground structure, *IET Microwaves, Antennas Propag.*, vol. 14, no. 2, pp. 215–226
- [4] C. Kumar, and D. Guha. (2015). Reduction in cross-polarized radiation of microstrip patches using geometry-independent resonant-type defected ground structure (DGS), *IEEE Transactions Antennas Propag.*, vol. 63, no. 6, pp. 2767–2772
- [5] C. Kumar, M. I. Pasha, and D. Guha. (2015). Microstrip patch with nonproximal symmetric defected ground structure (DGS) for improved cross-polarization properties over principal radiation planes, *IEEE Antennas Wirel. Propag. Lett.*, vol. 14, pp. 1412–1414
- [6] S. Biswas, C. K. Ghosh, A. Medda and D. Mandal. (2016). Harmonics suppression of microstrip patch antenna using defected ground structure. *International Conference on Microelectronics Computing and Communications (MicroCom)* (pp. 2–5). Durgapur, India
- [7] W.-C. Liu, C.-M. Wu, and Y. Dai. (2011). Design of triple-frequency microstrip-fed monopole antenna using defected ground structure, *IEEE Transactions Antennas Propag.*, vol. 59, no. 7, pp. 2457–2463
- [8] V. S. Kushwah and G. S. Tomar. (2011). Size reduction of microstrip patch antenna using defected microstrip structures. in *Communication Systems and Network Technologies (CSNT), 2011 International Conference on Communication System and Network Technologies*, pp. 203–207, Katra, India
- [9] N. K. Darimireddy, R. R. Reddy, and A. M. Prasad. (2018) .A miniaturized hexagonal-triangular fractal antenna for wide-band applications [antenna applications corner], *IEEE Antennas and Propagation Magazine*, vol. 60, no. 2, pp. 104–110
- [10] K. Wei, J. Y. Li, L. Wang, R. Xu, and Z. J. Xing. (2017). A new technique to design circularly polarized microstrip antenna by fractal defected ground structure, *IEEE Transactions on Antennas and Propagation*, vol. 65, no. 7, pp. 3721–3725
- [11] Y. Zhong, Y. Yang, X. Zhu, E. Dutkiewicz, K. M. Shum, and Q. Xue. (2017). An On-Chip bandpass filter using a broadside-coupled meander line resonator with a defected-ground structure, *IEEE Electron Device Lett.*, vol. 38, no. 5, pp. 626–629
- [12] S. Hekal, Adel B. Abdel-Rahman, Hongting Jia, Ahmed Allam, Adel Barakat, Takano Kaho, and Ramesh K. Pokharel. (2016). Compact wireless power transfer system using defected ground bandstop filters, *IEEE Microwave and Wireless Components Letters*, vol. 26, no. 10, pp. 849–851
- [13] Z. Zeng, S. J. Chen, and C. Fumeaux. (2019). A reconfigurable filter using defected ground structure for wideband common-mode suppression, *IEEE Access*, vol. 7, pp. 36980–36990
- [14] S. M. Han, C.-S. Kim, D. Ahn, and T. Itoh. (2005). Phase shifter with high phase shifts using defected ground structures, *Electronics Letter*, vol. 41, no. 4, pp. 196–197
- [15] S. Bayaskar, D. Brahme, and K. Shambavi. (2016). Compact rat race coupler with harmonic suppression using Circular defected ground structure (CDGS), *2016 International Conference on Global Trends in Signal Processing, Information Computing and Communication (ICGTSPICC)*, (pp. 316–319), Jalgaon, India
- [16] V. Kumar, and S. Gurjar. (2013). A tutorial overview on the DGS to design microwave Devices, *Proceedings of National Conference on Trends in Signal Processing & Communication (TSPC'13)*, (pp. 119–122) , India
- [17] J. X. Liu, W. Y. Yin, and S. L. He. (2010). A new defected ground structure and its application for miniaturized switchable antenna. *Progress In Electromagnetics Research*, vol. 107, pp. 115–128
- [18] J. S. Lim, Y. T. Lee, J. H. Han, J. S. Park, D. Ahn, and S. Nam. (2002). A technique for reducing the size of amplifiers using defected ground structure', *2002 IEEE MTT-S International Microwave Symposium Digest*, vol. 2, (pp. 1153–1156), Seattle, USA
- [19] P. R. Prajapati, G. G. K. Murthy, A. Patnaik, and M. V. Kartikeyan. (2015). Design and testing of a compact circularly polarised microstrip antenna with fractal defected ground structure for L-band applications, *IET Microwaves, Antennas Propagation*, vol. 9, no. 11, pp. 1179–1185
- [20] H. D. Oskouei, K. Forooghi, and M. Hakkak. (2007). Guided and leaky wave characteristics of periodic defected ground structures, *Progress In Electromagnetics Research*, *PIER*, vol. 73, pp. 15–27
- [21] C. A. Balanis. (2005). *Antenna Theory: Analysis and Design* (3rd ed.). Canada: John Wiley.
- [22] E. Van Nechel, F. Ferranti, Y. Rolain, and J. Lataire. (2020). An equivalent circuit model for wide-band analysis of defected ground structures with asymmetric slot and multiple slots, *Microwave and Optical Technolgy Letters*, pp. 1–7

- [23] H. Kaouach, L. Dussopt, and R. Sauleau. (2015). Modeling, design and demonstration for discrete lens antennas with circular-polarization in the 60-GHz band, *International Journal of Research in Wireless Systems (IJRWS)*, vol. 1, Issue 1, pp. 7–15
- [24] X. Shang and M. J. Lancaster. (2013). Patch antenna with integrated bandpass filter, 4th Annual Seminar on Passive RF and Microwave Components, (pp. 1–5), Birmingham, UK
- [25] R. Garg, P. Bhartia, I. Bahl, and A. Ittipiboom. (2001). *Microstrip antenna design handbook*. Artech house.
- [26] M. H. Badjian, C. K. Chakrabarty, S. Devkumar, and G. C. Hock. (2009). Lumped element circuit model approximation of an UWB patch antenna, *Proceedings of the 2009 IEEE 9th Malaysia International Conference on Communications*, (pp. 28–32), Kuala Lumpur, Malaysia
- [27] Hong, Jia-Shen G., and Michael J. Lancaster. (2001). *Microstrip filters for RF/microwave applications*, vol. 167. John Wiley & Sons.
- [28] K. S. Ahmad, S. A. Hamzah, and F. Che Seman. (2015). Defected ground structure for beam steering array antenna applications, *ARPN Journal Engineering and Applied Sciences*, vol. 10, no. 19, pp. 8653–8658
- [29] D. Ahn, J.-S. Park, C.-S. Kim, J. Kim, Y. Qian, and T. Itoh. (2001). A design of the low-pass filter using the novel microstrip defected ground structure, *IEEE Transactions on Microwave Theory and Techniques*, vol. 49, no. 1, pp. 86–93
- [30] J.-S. Park, J.-H. Kim, J.-H. Lee, S.-H. Kim, and S.-H. Myung. (2002). A novel equivalent circuit and modeling method for defected ground structure and its application to optimization of a DGS lowpass filter, in *Microwave Symposium Digest, 2002 IEEE MTT-S International Microwave Symposium Digest*, vol. 1, (pp. 417–420), Seattle, USA
- [31] N. C. Karmakar, S. M. Roy, and I. Balbin. (2006). Quasi-static modeling of defected ground structure, *IEEE Transactions on Microwave Theory and Techniques*, vol. 54, no. 5, pp. 2160–2168
- [32] C. Caloz, H. Okabe, T. Iwai, and T. Itoh. (2004). A simple and accurate model for microstrip structures with slotted ground plane, *IEEE Microwave and Wireless Components Letters*, vol. 14, no. 3, pp. 127–129
- [33] B. Mohamazade and M. Afsahi. (2017). Mutual coupling reduction and gain enhancement in patch array antenna using a planar compact electromagnetic bandgap structures, *IET Microwaves, Antennas & Propagation*, vol. 11, Issue. 12, pp. 1719–1725
- [34] G. Jin, M. Li, D. Liu, and G. Zeng. (2018). A Simple planar pattern-reconfigurable antenna based on arc dipoles, *IEEE Antennas Wireless Propagation Letters*, vol. 17, no. 9, pp. 1664–1668
- [35] H. N. Chu, G. Y. Li, and T. G. Ma. (2018). Planar pattern switchable antenna using phase reconfigurable synthesized transmission lines, *IEEE Antennas Wireless Propagation Letters*, vol. 17, no. 12, pp. 2319–2323
- [36] S. L. Chen, P. Y. Qin, W. Lin, and Y. J. Guo. (2018). Pattern-reconfigurable antenna with five switchable beams in elevation plane, *IEEE Antennas Wireless Propagation Letters*, vol. 17, no. 3, pp. 454–457
- [37] A. Darvazehban, S. A. Rezaeieh, O. Manoochchri, and A. M. Abbosh. (2020). Two-dimensional pattern-reconfigurable cross-slot antenna with inductive reflector for electromagnetic torso imaging, *IEEE Transactions on Antennas and Propagation*, vol. 68, no. 2, pp. 703–711
- [38] H. A. Majid, M. K. A. Rahim, M. R. Hamid, and M. F. Ismail. (2014). Frequency and pattern reconfigurable slot antenna, *IEEE Transactions on Antennas and Propagation*, vol. 62, no. 10, pp. 5339–5343
- [39] C. M. Lee and C. W. Jung. (2015). Radiation-pattern-reconfigurable antenna using monopole-loop for fitbit flex wristband, *IEEE Antennas Wireless Propagation Letters*, vol. 14, pp. 269–272
- [40] P. Lotfi, S. Soltani, and R. D. Murch. (2016). Broadside beam-steerable planar parasitic pixel patch antenna, *IEEE Transactions on Antennas and Propagation*, vol. 64, no. 10, pp. 4519–4524
- [41] S. N. M. Zainarray, N. Nguyen-Trong, and C. Fumeaux. (2018). A frequency- and pattern-reconfigurable two-element array antenna, *IEEE Antennas Wireless Propagation Letters*, vol. 17, no. 4, pp. 617–620
- [42] I. Lim and S. Lim. (2013). Monopole-like and boresight pattern reconfigurable antenna, *IEEE Transactions on Antennas and Propagation*, vol. 61, no. 12, pp. 5854–5859